# Multi-frame Elastography Using Handheld Force-Controlled Ultrasound Probe

Andrey Kuzmin, Aaron M. Zakrzewski, Brian W. Anthony, Victor Lempitsky

***Abstract*—We propose a new method for strain field estimation in quasi-static ultrasound elastography based on matching radio frequency (RF) data frames of compressed tissues. The method benefits from using a handheld force-controlled ultrasound probe, which provides the contact force magnitude and therefore improves repeatability of displacement field estimation. The displacement field is estimated in a two-phase manner using triplets of RF data frames consisting of a pre-compression image and two post-compression images obtained with lower and higher compression ratios. First, a reliable displacement field estimate is calculated for the first post-compression frame. Second, we use this displacement estimate to warp the second post-compression frame while using linear elasticity to obtain an initial approximation. Final displacement estimation is refined using the warped image. The two-phase displacement estimation allows for higher compression ratios, thus increasing the practical resolution of the strain estimates. The strain field is computed from a displacement field using a smoothness-regularized energy functional, which takes into consideration local displacement estimation quality. The minimization is performed using an efficient primal-dual hybrid gradient algorithm, which can leverage a graphical processing unit's (GPU) architecture. The method is quantitatively evaluated using finite element (FE) simulations. We compute strain estimates for tissue-mimicking phantoms with known elastic properties and finally perform a qualitative validation using in-vivo patient data.**

## I. INTRODUCTION

Ultrasound elastography is a technique that estimates the elastic properties of human tissue based on ultrasound imagery. This paper is focused on quasi-static elastography and targets tissue strain reconstruction from a sequence of radio frequency (RF) data frames.

Generally, there are many different elastography modalities. Common techniques include shear wave elastography, compression-based strain elastography, and compression-based quantitative elastography. Strain-based elastography offers advantages over shear wave elastography. For example, while shear wave elastography is computationally cheap, shear waves attenuate significantly in fluids. Thus, shear wave elastography is inaccurate near fluids, such as blood in an artery. The method presented in this paper has the advantage that it can be used even on tissue that appears to be under an artery in an ultrasound image. Further, the method presented in this paper is applicable to every existing 1D ultrasound probe; these probes are common, even in low-budget, underdeveloped areas of the world. Shear wave elastography requires a different imager and thus is less easily adoptable throughout the world.

Many compression-based quantitative elastography methods depend on an excellent estimation of strain in order to obtain an accurate elastogram. Thus, while the method presented in this paper can be used for qualitative strain elastography, the method can also be used to increase the accuracy of the existing quantitative techniques.

Despite the fact that some elastography techniques are commercially available, there is significant room for improvement. Given the potential world-wide adoptability of strain-based elastography, there is a need for improving the imaging quality and the reproducibility of strain elastography via new acquisition principles, new hardware designs, and via better image reconstruction algorithms.

Here, we describe a new strain elastography method that improves conventional strain elastography in a number of ways. The main improvement is obtained via the use of the *triplets* of RF frames with known ratio of compression levels (as opposed to pairs of frames matched by the majority of the proposed methods). The compression ratios are obtained using a force-controlled ultrasound probe as proposed in [1], [2]. Such probes were recently created to increase control of the imaging process. This has particular benefits for elastography imaging, which is more operator-dependent compared to ultrasound imaging. The probe used in our experiments can apply a prescribed contact force magnitude, and furthermore can maintain a graduated force range during the acquisition of image sequences. This hardware setup naturally suggests the development of multi-frame elastography algorithms employing contact force values to improve the quality of strain estimation. Alternatively, our approach can be applied to RF triplets obtained with a conventional non-force-controlled probe, in which case the force ratio can be estimated algorithmically. This scenario however requires additional processing time, and generally makes the success of the approach more dependent on the operator.

As a part of our approach, we propose a strain reconstruction algorithm that processes the acquired triplets of RF frames. During the first stage, the algorithm uses a pair of frames with small relative deformation to estimate a coarse displacement field. This displacement field is magnified according to the estimated force ratio, and is used as an initialization for the second stage that considers a pair of frames that exhibit larger relative deformation. This second pass of the algorithm relies on a new formulation of the functional for strain estimation that imposes total variation (TV) regularization on the estimated strain fields and permits graphical processing units (GPU)-accelerated primal-dual optimization.

We evaluate the proposed approach in the series of experiments with synthetic phantoms, for which the ground truth displacement fields can be estimated with high accuracy using finite-element (FE) modeling. We also consider experimental gelatin-agar phantoms with known geometry. Based on the experiments, we conclude that our method can compute smooth strain estimates for up to two times higher tissue compression ratios compared to the two-frame algorithm leading to an increase in the spatial resolution. The results are supported by in-vivo human tissue experiments, which demonstrate that the method can resolve additional features within the obtained strain fields, as the application of a greater contact is enabled by the proposed method. Our results further justify the use of force-controlled ultrasound probes and demonstrate their particular utility for strain elastography.

## II. BACKGROUND

Most existing methods estimate the strain by computing the spatial derivatives of the displacements between a pair of ultrasound frames with different compression levels. A number of approaches [3], [4] estimate the displacements based on cross-correlation block matching. In the absence of regularization, such methods usually produce noisy displacement fields. Significant improvement of the block matching algorithm were proposed in [5] by combining several techniques including quality determined search, automatic search range and adaptive block size.

Several published methods are based on discrete optimization, where objective functions combine a data fidelity term with a first-order displacement continuity prior. For example, the method introduced in [6] is based on a functional with a first-order smoothness term that is minimized using dynamic programming (DP). The bias towards constant strain introduced by the binary smoothness term is eliminated by using refinement based on continuous optimization; however, the method assumes a limited magnitude of lateral displacements as a result of using a greedy strategy for lateral displacement search. Another representative work [7] uses a multi-scale iterative conditional mode (ICM) algorithm to minimize a similar functional that incorporates a first-order spatial smoothness prior on the displacement field. The method converges to a local minimum, and therefore the result depends on the quality of initial estimate obtained by the unregularized coarse-scale search. For large compression levels, in our experience, the method is likely either to find an overly smooth local minimum that misses important details or to diverge (i.e. to find a highly non-smooth minimum) as the coarse-to-fine optimization progresses.

To provide clinically-useful visualization, one has to turn an estimated displacement field into a strain field, which requires computing the gradient of noisy data. A classical approach is to use least-squares robust fitting as proposed in [8]. A comprehensive overview of existing strain estimation methods is given in [9] and includes several methods using spline fitting and wavelet denoising for computing robust derivative [10], [11]. Strain estimation can also be formulated as an inverse problem where an anti-differentiation operator is used to describe the relation between the displacement estimation and a regularized strain field [12]. Another family of robust methods estimate strain as a local compression rate and employ a normalized-cross correlation (NCC) search in the frequency domain to reduce the computational complexity [13].

The most challenging task in strain estimation is thus to find a natural, but sufficiently smooth approximation to the displacement field between two RF data frames. In many cases, ultrasound images contain significant noise level so that the conventional block-matching search algorithms are likely to produce noisy displacement estimates. The quality of the estimates highly depends on the complexity of tissue structures and the degree of compression. In practice, it is very hard to find reliable displacement estimates for most real tissues undergoing 2-3% compression unless special techniques are introduced. However, higher compression ratios up to 5% lead to emergence of additional features in the strain images and therefore provide greater diagnostic capabilities.

Most of the methods aiming for motion tracking for high compression rates introduce a spatial smoothness prior for the displacement field [7], [14]. Thus, the trade-off between the spatial smoothness and physical relevance of the solutions is introduced. In a number of cases it is only possible to find a smooth displacement field at the cost of introducing over-smoothed non-physical solutions that are favourable for visual inspection, but may neglect important tissue structures or even contain information that is not actually represented in the real tissue.

Arguably, the most promising way to compute a reliable displacement estimate for higher compression rates is to warp RF data frames using some smooth initial displacement estimate thus effectively decreasing the compression ratio before an attempt to use a displacement estimation algorithm. This technique has been used under the name *companding* in order to introduce a two-step coarse-to-fine displacement search algorithm for two-frame elastography [15]. A related approach benefits from RF data warping by computing a robust strain estimate directly as a local compression rate [13]. A coarse initial displacement estimate is used for warping.

It is possible, however, to improve the quality of the displacement estimation by using more than two images. In [16] a sequence of RF data frames is used for strain estimation. Consecutive realignment of the displacement field maintains a reliable displacement estimate while gradually progressing from small to large compression rate. Another approach is to employ three frames and using linear elasticity for an initial approximation while softly penalising deviations from linear elasticity using a first-order smoothness prior [14]. However, the explicit bias towards the linear solution might be undesirable for clinical applications, and is avoided in our approach that instead uses the linear elasticity assumption solely for the initialization and for limiting the search range, while avoiding any explicit biases within the search range.

## III. DISPLACEMENT ESTIMATION

There are several main sources of nonlinearity between contact force and strain in quasi-static elastography. The first is mechanical i.e. the fact that the strain is underestimated in most tissues if linear elasticity is assumed. The presence of pressure sources such as blood vessels and arterial walls represents another source of non-linearity. Finally, the operator dependent application of the contact force including spontaneous rotation and out-of-plane motion of the ultrasound probe often lead to non-trivial deformations even for smaller compression rates. The above-mentioned considerations suggest the development of a new algorithm that benefits from assuming linear elasticity, but considers it only as an initial approximation and therefore has the potential to handle more sophisticated spatial strain dependencies and motion patterns.

We start the discussion of the algorithm by introducing the notation. We assume a triplet of RF data frames $\{I_0, I_1, I_2\}$ is given. Each data frame has $m$ signals sampled at $n$ points, i.e. it can be regarded as an $m \times n$ image. Each pair of RF frames can be related by a displacement field $d(p) = d(x, y) = (d_a(x, y),\ d_l(x, y))$ assigning a $2D$ displacement field to each pixel $p = (x, y)$ of the first frame. Thus, it is assumed that the pixel $p$ in the first frame is matched to the pixel $p - d(p)$ in the second frame. Here, $d_a$ and $d_l$ denote the axial and the lateral components of the displacement respectively. Our final goal, however, is to reconstruct a smooth estimate for the in-plane normal *strain* field $s(x, y) = (s_a(x, y),\ s_l(x, y))$. We do not estimate shear strains and out-of-plane normal strains. The relation between the two fields of interest is discussed below.

For each post-compression RF data frame, we search for the values of the displacement vector within a discrete configuration set $\Lambda$ (search window) that is defined for each image as follows:

$$\Lambda = \{0, \ldots, +D_a\} \times \{-D_l, \ldots, +D_l\}\,. \tag{1}$$

Here $D_a$ and $D_l$ are the maximum authorized values of displacement in the axial and in the lateral direction respectively.

We start our algorithm by computing a reliable displacement field estimate for moderate compression ratio of approximately $1\%$. A standard block matching architecture followed by the median filter is used (the median filter step is needed in order to eliminate spurious matches). The force magnitude is chosen so that a smooth displacement estimate with the minimal amount of outliers is produced. Overall, the first block matching procedure can be summarized with an equation:

$$d_{coarse} = \texttt{BlockMatch}(I_0, I_1)\,, \tag{2}$$

where `BlockMatch` denotes the block matching displacement estimation algorithm which takes a pair of RF data frames (pre-compression and post-compression) as an input and produces a 2D displacement field as an output, and $d_{coarse}$ denotes the displacement field estimated for the $(I_0, I_1)$ RF image pair.

As the ultrasound probe we use provides the contact force values on the fly, we multiply the first displacement estimate by a value, given by a relative force corresponding to the compression ratio of the remaining RF image $I_2$ (typically 2-3$\%$ percent of compression). Thus we obtain an initial displacement estimate for the $(I_0, I_2)$ image pair as $\frac{f_2}{f_1}\, d_{coarse}$. We then use the obtained estimate to warp the RF data frame of $I_2$.

Finally, we run the displacement search between $I_0$ and the warped version of $I_2$, which we denote as $\texttt{Warp}(I_2, \frac{f_2}{f_1}\, d_{coarse})$. Here, we once again use a simple block matching, but with a very narrow search range. Limiting the range of the search in this case reduces the probability of making spurious matches considerably. Overall, the second matching can be summarized by the following equation:

$$d_{local} = \texttt{BlockMatch}\left(I_0, \texttt{Warp}(I_2, \frac{f_2}{f_1}\, d_{coarse})\right) \tag{3}$$

Given $d_{coarse}$ and $d_{local}$, the displacement field between $I_0$ and $I_2$ can be estimated using a simple sum:

$$d_{total} = \frac{f_2}{f_1}\, d_{coarse} + d_{local} \tag{4}$$

The total displacement is given as an input for the strain estimation algorithm.

In the block matching computations, we use the sum of squared differences (SSD) as a similarity measure for the block-matching search. As an additional information that is passed to the strain estimation, we find the block-matching quality measure $q_{ij}$ that is computed for each pixel after the displacement field estimation as the normalized SSD difference measure for the corresponding patches of RF data frames.

Once again, note that we use the linear elasticity assumption only as an initial approximation as opposed to [14]. We allow limited deviations from the linear elasticity model, and do not penalize such deviation.

## IV. STRAIN ESTIMATION

### A. *Energy functional.*

One of the challenges of the ultrasound elastography is to compute a tissue strain estimate given the displacement field value. The displacement estimation often suffers from high noise level and significant amount of outliers disabling direct usage of conventional gradient-based techniques for numerical differentiation. Although this topic was a subject for extensive research, there is still a room for adoption of recent advances in image denoising and inverse problems [17], [18], [19], [20] which is one of the focuses of this paper.

Since ultrasound images have poor lateral resolution, we do not perform lateral strain estimation. Following [9] we treat the axial strain estimation as the inverse problem and consider the energy functional of the form:

$$E(s) = ||As - d_a|| + \lambda\rho(s) \tag{5}$$

where $s$ is the smooth estimate of the axial strain, $\rho(s)$ is a regularization term and $\lambda$ is a regularization parameter. In the simplest case, the strain field thus equals the spatial derivative of the displacement field. However, in the presence of noise, a more numerically stable alternative for this formula is needed. Towards this end, one can relate the axial strain field to the axial displacement field using the spatial integration operator $A$ i.e. the prefix sum along each vertical line:

$$As + d_a(0) = \int_0^L s(x)dx + d_a(0) = d(L) \tag{6}$$

Given the fixed displacement estimate, the energy minimization over the strain variables is a convex optimization problem, which yields a global minimum. The quality of the solution typically depends on the choice of the smoothness prior.

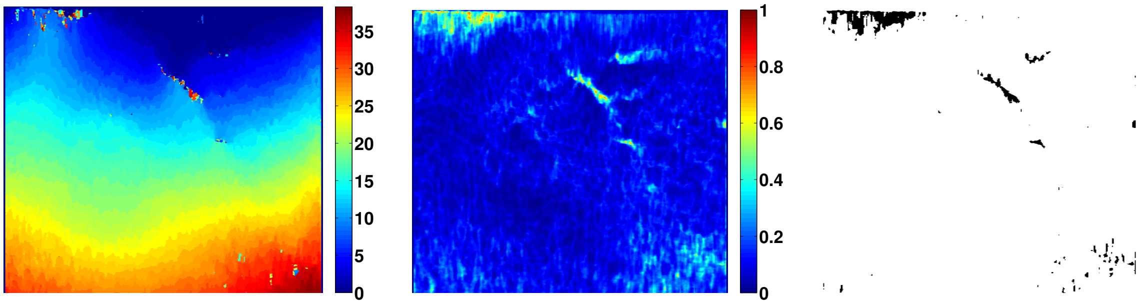

Displacement field Block matching quality Poorly matched pixels

Fig. 1. Example of SSD block matching quality field computed for human liver tissue (an example provided by the authors of [14]).

We observed that in many cases, estimated displacement fields still exhibit gross errors, especially at the tissue boundaries. Even a small patch of erroneously estimated displacements can result in an incorrect and highly discontinuous strain estimation. Fortunately, the regions where gross matching mistakes are likely to be reflected on the SSD score map $q_{ij}$ (see Figure 1). This allows to discard the matches and reconstruct strain values in the regions with high SSD score using the smoothness prior only. We show the example of the SSD score map aligned with the corresponding binary mask and the axial displacement field (figure 1). In order to incorporate this information into the energy functional, we introduce the diagonal matrix $D = diag(w)$ which discriminates the regions with high normalized-SSD matching score:

$$E(s) = ||D(As - d_a)|| + \lambda\rho(s) \tag{7}$$

The cost of the evaluation of the product $As$ within (7) may be excessive since the matrix $A$ has many (about a half of) non-zero entries. Since the strain estimation is local in its nature, the computational overhead of the strain integration can be potentially reduced by limiting the integration interval to some neighbourhood of the current sample. In our experience, visually indistinguishable results are obtained for the strain field if a vertical 100-sample neighbourhood is used and a finite-difference operator with the same interval is applied to the axial displacement field prior. However, since optimized parallel versions for the prefix sum (`cumsum`) described in the next section are provided, we keep the original formulation for the sake of simplicity.

We use a binary weight $w$ for each pixel based on the thresholded score $q_{ij}$ in order to separate the regions of presumably low and high confidence of the match:

$$w_{ij} = \begin{cases} 1 & q_{ij} < t \\ 0 & \text{otherwise} \end{cases} \tag{8}$$

Thus, the regions with $w_{ij} = 0$ correspond to pixels, where the estimated displacement is deemed unreliable, and where smoothness-based interpolation is used during the strain reconstruction.

### *B. Regularization.*

**Quadratic smoothness prior.** One of the conventional ways to enforce smoothness of the strain field is to explicitly penalize its spatial variations:

$$E(s) = ||D(As - d_a)||_2 + \int \left(\alpha[D_x s]^2 + [D_y s]^2\right) , \tag{9}$$

where $D_x$ and $D_y$ are the first order finite difference operators for the corresponding coordinate axes. Since the physical dimensions of each sample in an RF data frame vary by an order of magnitude for axial and lateral components, we introduce the coefficient $\alpha$ in order to equally penalize the spatial variations in each direction. The functional is minimized using the least squares method, which is performed by solving a sparse linear system.

**Anisotropic TV prior.** The well-known problem with the quadratic smoothness prior is the associated blurring of the boundaries, and Total Variation (TV) regularization is a popular alternative addressing this problem [21]. When considering the anisotropic TV-norm as a regularization of choice for the problem, the energy equals to:

$$E(s) = ||D(As - d_a)||_2 + \lambda TV_\alpha(s) \tag{10}$$

where the second term is expressed as:

$$TV_\alpha(s) = \int \sqrt{\alpha[D_x s]^2 + [D_y s]^2} \tag{11}$$

Using TV-prior allows the preservation of discontinuities on the boundary between hard and soft tissues. As efficient primal-dual methods were introduced for the Rudin-Osher-Fatemi (ROF) model [21], we consider the TV-L2 functional as a good choice due to faster implementations compared to affine-preserving generalization of TV introduced in [17], [19].

The dual version of the anisotropic TV-norm is introduced as follows:

$$TV_\alpha(u) = \sup\{\int u \text{ div }_\alpha v, ||v||_\infty \leq 1\} \tag{12}$$

We then use the anisotropic versions of conjugate divergence and gradient operators

$$\text{div }_\alpha v = \alpha\frac{\partial v_1}{\partial x_1} + \frac{\partial v_2}{\partial x_2} \tag{13}$$

$$\nabla_\alpha v = \left(\alpha \frac{\partial v_1}{\partial x_1}, \frac{\partial v_2}{\partial x_2}\right) \tag{14}$$

These operators are chosen to be adjoint to each other, i.e. :

$$(\text{ div }_\alpha)^* = -\nabla_\alpha \tag{15}$$

### C. Optimization.

Following [18] we employ the primal-dual algorithm to our minimization problem. We omit the diagonal matrix $D$ for the sake of simplicity and rewrite the energy expression as a convex-concave saddle-point problem:

$$\min_{s \in S} \max_{p \in P, r \in R} \langle \nabla s, p \rangle + \langle As - d, r \rangle - \frac{\lambda}{2} ||r||_2^2 \tag{16}$$

Where $p$ and $r$ are the dual variables with respect to $s$ and the residual $(As - d)$ respectively. The unit balls $P$ and $R$ associated with these variables, e.g..:

$$P = \{p \in C^{2mn}, ||p||_\infty \leq 1\} \tag{17}$$

We also define the following proximal map:

$$\text{prox}_2^\sigma(\tilde{r}) = \arg\min_{r \in R} \frac{||r - \tilde{r}||_2^2}{2\sigma} + \frac{\lambda}{2} ||r||_2^2 = \frac{\tilde{r}}{1 + \sigma\lambda} \tag{18}$$

The minimization is performed as follows:

$$s = 0, p = 0, r = 0, \text{choose } \tau, \sigma > 0 \tag{19}$$

The update rules [19] in every iteration are given by:

$$p = \text{proj}_P(p + \sigma \nabla s) \tag{20}$$

$$r = \text{prox}_2^\sigma(r + \sigma(As - d)) \tag{21}$$

$$s = s + \tau(\text{div} p - A^* r) \tag{22}$$

We repeat the procedure until convergence of s. The optimal choice of the step-size is of great importance for numerical performance of the algorithm. We adopted the strategy described in [20] and use the rules for computing $\tau$ and $\sigma$ for the iteration $n$:

$$\sigma_n = 0.2 + 0.08n \tag{23}$$

$$\tau_n = \left(0.5 - \frac{5.0}{15.0 + n}\right) \tag{24}$$

It is necessary to use consistent discretizations for the gradient and divergence operators [17]. We use the following definition based on the first-order finite differences:

$$\text{div} v = \delta_{x+} v_1 + \delta_{y+} v_2 \tag{25}$$

$$\nabla u = (\delta_{x-} u_1, \delta_{y-} u_2) \tag{26}$$

where the $\delta_{x+}, \delta_{y+}$ and $\delta_{x-}, \delta_{y-}$ correspond respectively to the forward and the backward finite-difference operators.

| force<br>(direct measurement) | force<br>(indirect measurement) | relative error |
|---|---|---|
| 1.61 | 1.51 | 6% |
| 1.68 | 1.68 | 0% |
| 1.75 | 1.86 | 6% |
| 1.75 | 1.84 | 5% |
| 1.80 | 1.90 | 6% |
| 1.86 | 1.76 | 5% |
| 2.36 | 2.21 | 6% |

TABLE I. Indirect force measurement error. The table shows comparison of the force values obtained in two different ways: the first column contains values provided the force-controlled probe whereas the second column contains the algorithmically obtained estimation. The results suggest average 5% error for the estimated force values considering the probe-provided values as reference.

### D. GPU implementation.

The primal-dual algorithm described in the previous section can be parallelized at the pixel-wise level, since most of the operations only need the values of the neighbouring pixels in every iteration. Such algorithms are naturally mapped to data-parallel GPU architectures that support SIMD (single-instruction, multiple data) instructions.

Active use of the local memory is among the most important aspects of the parallel implementation. We developed our own efficient kernel for dual update that loads small patches of the frame into local memory, performs one iteration and writes the patch to the global memory. Fast access to the local memory is performed block-wise in each iteration.

The bottleneck part of our GPU implementation is the computation of the prefix sums. The product performed within the update in (21) is simply computed column-wise whereas update in (22) requires computing the product with the transposed matrix of this operation. Such an operation is computed within three steps. The image is flipped vertically, then the column-wise prefix sum is computed for each vertical column and finally the product is flipped vertically once again. We use an optimised implementation of the prefix sum and flip operations provided by NVIDIA `Thrust` library [22] to perform the operation in three steps. Data parallel versions of floating point vectors from the library are used to compute pixel-wise linear combinations in the updates in (21) and (22).

The energy computation requires performing parallel gather operations constituting significant computational burden for GPU architectures. Therefore it is beneficial to compute energy only once in 100 iterations reducing the total time required for practical convergence.

## V. Experimental validation

Below we are reporting the quantitative and the qualitative performance of the methods in a range of experiments spanning from the fully synthetic experiments with known ground truth to in vivo data, for which only qualitative assessment is possible. Generally, we restrict our comparison to the axial strain maps, which have the largest diagnostic value.

**Compared methods.** In the following section, we compare five methods. Four of them can be seen as variations of our approach. They correspond to two types of smoothness priors (quadratic and TV) and two types of input data (triplets vs. pairs). Given a pair of RF images as an input, we simply run the block matching algorithm discussed above and then use the obtained displacement map to estimate the strain field (i.e. we follow the standard pipeline used in a number of previous approaches [13], [23], [6]).

To compare with the method that is not based on block matching, we also evaluated a strong baseline based on estimating displacement field using dynamic programming (DP) and then applying TV-regularized smoothing to its derivative. The method is therefore similar to several previous works [24], [25], [6]. While implementing this baseline method, we made an effort to tune all parameters to obtain optimally looking results on the test data.

We now discuss the experimental data and protocols, as well as the obtained results.

**Indirect contact force measurement.** In general, our method is applicable for any freehand scans unless significant probe rotation is introduced. We conducted a series of experiments in which we measure the relative value of the contact force directly and algorithmically. For the purpose of the latter we find the noisy axial displacement estimate for eight post-compression frames relative to the same pre-compression frame. We consider the axial displacement for the least compressed frame as a unit displacement. The ratio of each of the seven remaining post-compression frames relative to the unit value is computed for each pixel. Finally the median value of the ratio is reported as the force value measured indirectly. Table I contains values of forces measured directly and algorithmically compared to each other for a series of 8 scans of a real gelatin-agar phantom.

The relative error introduced by the indirect force measurement is $5\%$ according to our experiments whereas the relative error for the physical force measurement is reported to be in the range of $2\%$. Thus, our method can be used for free-hand scanning, however the search range for the second block-matching phase has to be extended, which potentially leads to the increase in the number of outliers and the decrease in the quality of the strain estimation. The total computational complexity of the method in this scenario also increases since the additional displacement search phase is introduced.

**Synthetic phantom experiment.**

The commercially available finite element program `Abaqus` (Dassault Systmes, France) estimates the displacement fields corresponding to progressively increasing compression levels (up to 5 % compression in the axial direction).

In the finite element model, the material is linear elastic with a Poisson ratio of 0.495. A 2D formulation is used and the mesh consists of 4-node quadrilateral elements. This paper uses the common assumption in the elastography literature that the plane strain assumption is valid. The assumption assumes that the loading is chiefly within the plane of interest, which is likely to be approximately accurate because the operator is pushing vertically. We ignore out of plane forces and torques applied by the ultrasound probe on the skin surface. The assumption, as used by many in the literature, also assumes that out of plane strains are negligibly small. The finite element analysis uses a large deformation formulation so that the displacements are not limited to be infinitesimal. Equivalently, the formulation is geometrically non-linear.

In the finite element analysis, a 63.5 mm (horizontal dimension) by 48.75 mm (vertical dimension) phantom is simulated. A vertical displacement is applied at the bottom of the phantom. The nodes on the bottom of the phantom are enforced to be zero in the horizontal dimension. A stationary, rigid, 40 mm long ultrasound probe is centered upon and touches the top of the phantom. The center top node is constrained in both dimensions, while the nodes touching the probe are allowed to move horizontally. The nodes on the top of the phantom that are not touching the probe are free. The left and right sides of the phantom are free. No forcing is applied in the finite element model; the source of deformation is the prescribed displacement described above. The resulting deformation is such that the tissue near the ultrasound probe does not move vertically, and the tissue at the bottom of the phantom has the largest displacement; this is consistent with how an ultrasound image appears while a tissue is compressed.

In this experiment, we use a virtual phantom with six stiff inclusions of diameter 6, 4, 2, 1, 0.5, and 0.25 mm placed on an axes that was parallel to the ultrasound beam and the compression direction. In the six inclusion phantom, the inclusions have an elastic modulus of 30 kPa and the background material has an elastic modulus of 15 kPa. The nature of vertically aligned inclusions dictates that each inclusion will see a different amount of displacement. For the normal strains considered here, the axial strain can be thought of as the derivative of axial displacement in the axial direction. For this reason, the strain encountered by each inclusion should be similar. These displacement fields (and the corresponding strain maps obtained by differentiation) serve as the ground truth in our experiment. Using the virtual phantom and the obtained displacement fields, we use a popular ultrasound image simulation software Field-II [26], [27] to obtain a simulated RF data frames of resolution $3400 \times 128$.

As one of the target applications in elastography is tumour detection, we measure the suitability of the obtained strain maps for tumour delineation. To measure such suitability, we consider the simplest segmentation algorithm i.e. thresholding, in order to extract the regions of low strain that potentially represent hard inclusions. Following the thresholding, a connected component that has the largest overlap with the ground truth tumour shape is considered, and the standard Jaccard similarity measure between the ground truth shape and the shape of the picked connected component is evaluated:

$$J(A,B) = \frac{|A \cap B|}{|A \cup B|}$$

Since only the largest three inclusions are detected by the considered methods, we report the three Jaccard indices corresponding to the those three inclusions (Table II). The optimal threshold value is chosen independently for each method and for each of the inclusions (to maximize the Jaccard measure). The segmentation results for the synthetic phantom are shown in figure 3. After experimenting with different compression levels, we found that for the methods based on pairs of frame,

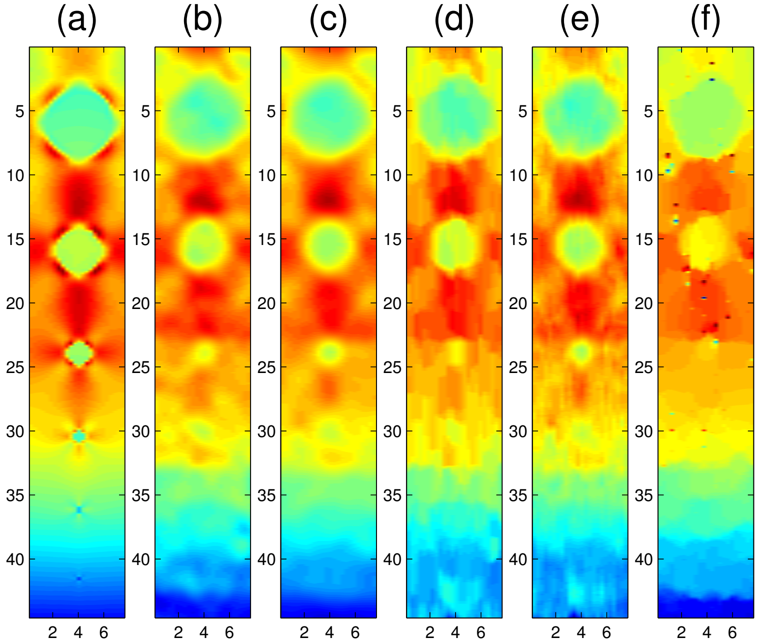

Strain images for the virtual phantom with 6 inclusions.

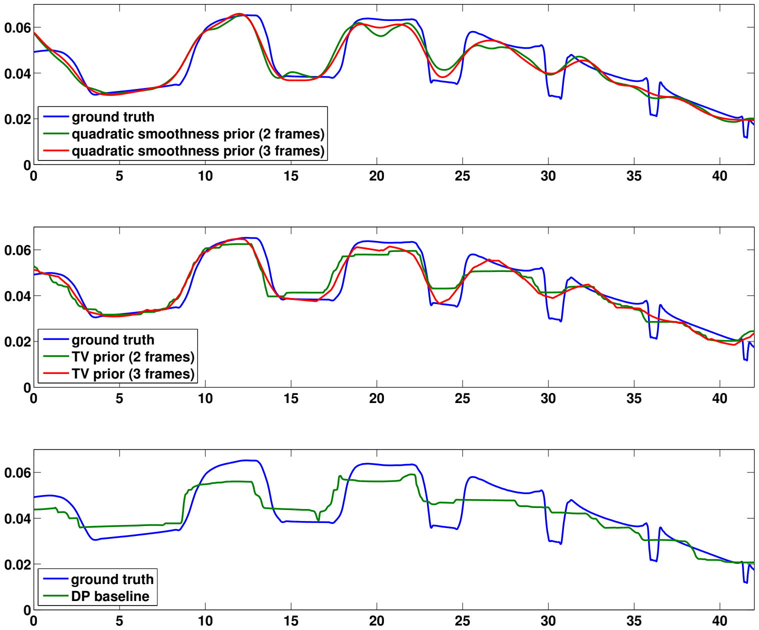

One-dimensional profiles of the strain estimates along the central vertical line

Fig. 2. Strain estimation for the virtual phantom with hard spherical 6 inclusions: (a) ground truth, (b) quadratic smoothness prior (2 frames), (c) quadratic smoothness prior (3 frames), (d) TV prior (2 frames), (e) TV prior (3 frames), (f) DP baseline. The strain profiles demonstrate benefit of using triplet-based displacement estimation algorithm. The proposed method demonstrates better performance compared to DP baseline when using both variants of the smoothness prior.

| Method | 6 mm | 4 mm | 2 mm |
|---|---|---|---|
| DP baseline | 81.1% | 66.2% | 57.0% |
| TV prior (2 frames) | 77.7% | 77.8% | 84.0% |
| TV prior (3 frames) | 80.4% | 81.4% | 86.0% |
| quadratic smoothness prior (2 frames) | 78.5% | 75.5% | 69.9% |
| quadratic smoothness prior (3 frames) | 80.9% | 78.5% | 87.2% |

TABLE II. JACCARD INDEX FOR THREE HARD INCLUSIONS. TRIPLET-BASED MATCHING GIVES SUPERIOR RESULTS.

| Method | average Jaccard index | average L2 error |
|---|---|---|
| TV prior (2 frames) | 31.0% | $7.0 \cdot 10^{-2}$ |
| TV prior (3 frames) | 40.5% | $5.9 \cdot 10^{-2}$ |
| DP baseline | 25.6% | $27.6 \cdot 10^{-2}$ |
| quadratic smoothness prior (2 frames) | 34.6% | $6.4 \cdot 10^{-2}$ |
| quadratic smoothness prior (3 frames) | 41.0% | $5.5 \cdot 10^{-2}$ |

TABLE III. QUANTITATIVE COMPARISON OF DIFFERENT METHODS FOR THE SET OF 7 SIMULATED PHANTOMS CONTAINING STIFF INCLUSIONS WITHIN LAYERED TISSUES.

compressing the second frame by 1% is nearly optimal, while for triplet-based estimation we further added a third frame compressed by 3%.

The results suggest that the triplet-based estimation outperforms the pair-based estimation and the DP baseline (figure 2). Thus, the results are improved when more distant frames (3% compression ratio) are considered and effectively matched.

**Set of synthetic phantoms with random geometry** As human tissue exhibits a layered structure (e.g. layers of muscle, fat or skin), one of the important aspect of elastography methods is to detect tumours, i.e. soft and hard inclusions, located within layers of different stiffness or on the boundary between two layers. In order to measure relative performance of the considered methods, we simulated a set of 7 phantoms with 4 circular inclusions each (three are shown on figure 4).

Each layer has a random thickness, constrained in a 44.45 mm height phantom. The coordinates of the inclusions are also random, constrained to not overlap with boundaries of the phantom. Each phantom consists of a 5 kPa layer, a 10 kPa layer, a 50 kPa layer, and a 120 kPa layer, each assigned to a randomly selected layer. Inclusions are circular, 2 mm in diameter and have an elastic modulus of 30 kPa. Each layer is simulated as an area of finite elements that have a different elastic modulus than the surrounding material. The mesh is consistent throughout the entire domain and nodes at the boundary between layers are part of elements in both of the surrounding layers.

First, we computed the strain estimates using pairs of pre-compression and 1% compressed RF data frames. We refer to these results as '2 frames' in the remaining part of this section. Second, we computed the strain estimates using triplets of pre-compression, 0.5% compression and 3.0% compression images, these results are referred as '3 frames'.

In the following table we report two error measures for the set of 7 phantoms (28 inclusions total): the average Jaccard index (same as above) and the average L2 error of the strain value for a square of 2.5 mm size surrounding each of the circular inclusions (Table III). We also show the cumulative error histogram, i.e. the fraction of the inclusions having error less than a certain value for both measures (Figure 6).

Overall, in the experiments with known ground truth, we observed a clear advantage of the triplet-based estimation with the proposed algorithm over the pair-based estimation. Both triplet-based estimation and pair-based estimation performed considerably better in all measures than the DP baseline.

According to quantitative measures, there was no advantage in using TV-smoothness prior over a simpler quadratic prior. Qualitatively, however, it can be observed that TV-smoothness results in sharper boundaries (figure 5), which can lead to a better delineation of stiff inclusions.

**Real gelatin-agar phantoms.** Our next set of experiments were performed using real phantoms. Gelatin (300 bloom, Porcine skin, Type A, Sigma-Aldrich, MO USA) and agar (Alfa-Aesar, MA USA) were used to make the phantoms using a process similar to that described in [28]. Graphite particles (crystalline, -300 mesh, 99%, Alfa Aesar, MA USA) were used as scatterers[1].

A Terason 3000t ultrasound system was used with a Terason 7L3-V ultrasound probe at 5 MHz during the phantom tests. The Terason Software Development Kit (SDK) captures radio frequency (RF) data from the probe and an attachment to the probe measures and records the force applied by the probe on the phantom [29].

The results of the evaluated methods (Figure 7) demonstrate the ability to visualize soft inclusions of a size down to 4 mm with a high degree of confidence using a standard approach based on two RF data frames with the TV prior on the strain field and the compression rate of 1%. Using the proposed triplet-based matching algorithm allows to increase the compression rate range from 1% to 2% whereas a direct computation of the displacement field between the uncompressed and the 2%-compressed image in such cases would introduce severe artifacts on the strain field (figure 7-bottom). As a result of using higher compression rates, the method allows to detect lesions of 2 mm size which would not be feasible with the pair-based variant of our algorithm.

**In-vivo human tissue experiment.** The RF data used in the experiment is acquired for a patient with liver cancer before ablation using an Antares Siemens system (Issaquah, WA) ultrasound machine. The sequence of images shows the tumor and was acquired by applying the contact force at a frequency of approximately 1 compression per 2 sec. The compression levels of 1.5% and 3.0% were used for the triple-based strain estimation method. The data that was first used in [14] was kindly provided by Dr. Hasan Rivaz. The relative forces values were measured algorithmically demonstrating the suitability of our method for images obtained with standard probes.

---

[1] Cylindrical phantom molds, with diameter of 94.45 mm, were machined using aluminum. A small cylindrical rod was used as a placeholder for the inclusion. By increasing the diameter of the rod, the diameter of the inclusion could be increased. The bulk material was poured into the mold and was allowed to solidify. Next, the small cylindrical rod was pulled out of the phantom and the resulting void was filled with the inclusion material. The resulting phantom had a height of approximately 55 mm. Experimental tests were carried out within 24 hours of phantom solidification.

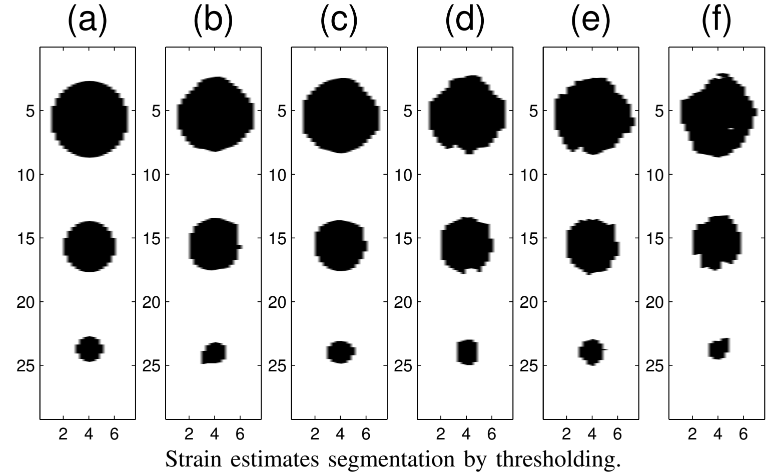

Fig. 3. Segmentation results for the virtual phantom with hard circular 6 inclusions: (a) ground truth, (b) quadratic smoothness prior (2 frames), (c) quadratic smoothness prior (3 frames), (d) TV prior (2 frames), (e) TV prior (3 frames), (f) DP baseline. The results confirm the benefit of using the triplet-based strain reconstruction. The proposed method achieves better segmentation quality compared to the baseline. Quadratic smoothness prior demonstrates slightly better results compared to TV prior for circular inclusions and both produce better results when the triplet-based algorithm is used.

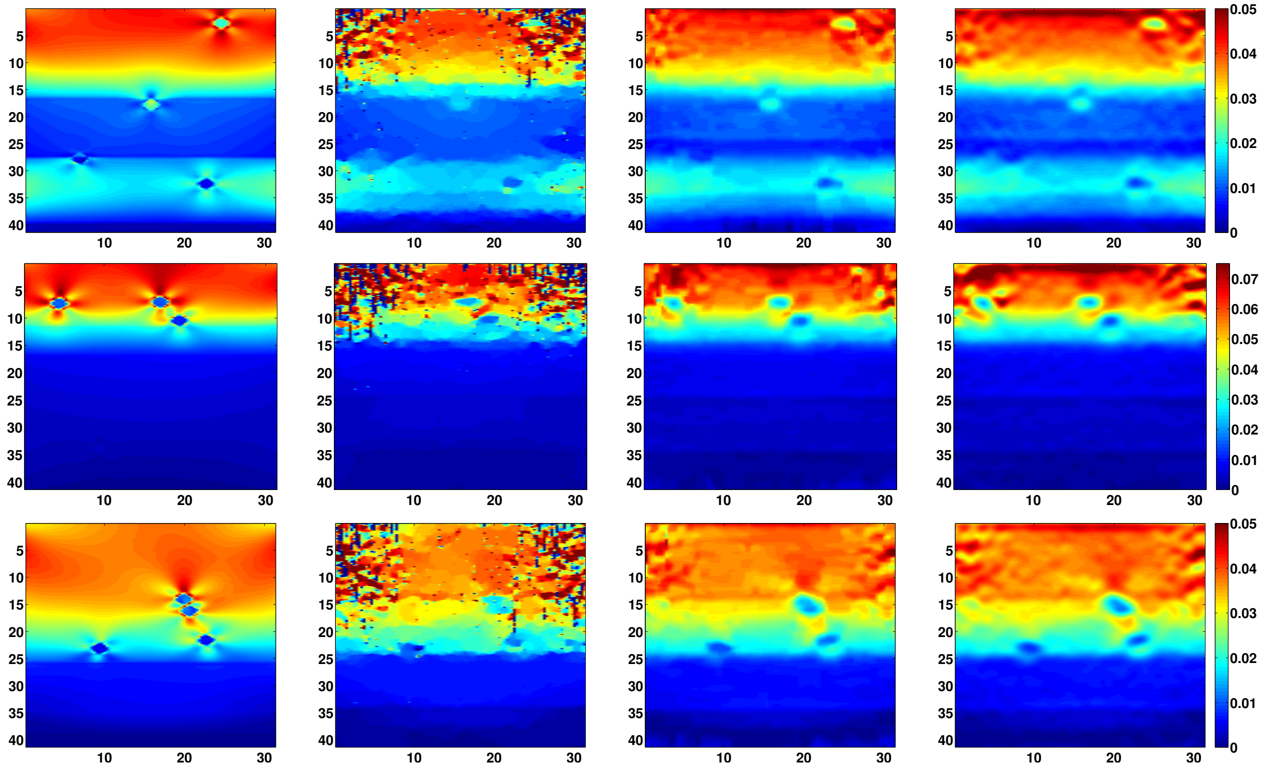

Fig. 4. Strain estimates for three synthetic phantoms with random geometry. Columns from the left to the right: (a) ground truth, (b) DP baseline, (c) TV prior (3 frames), (d) quadratic smoothness prior (3 frames)

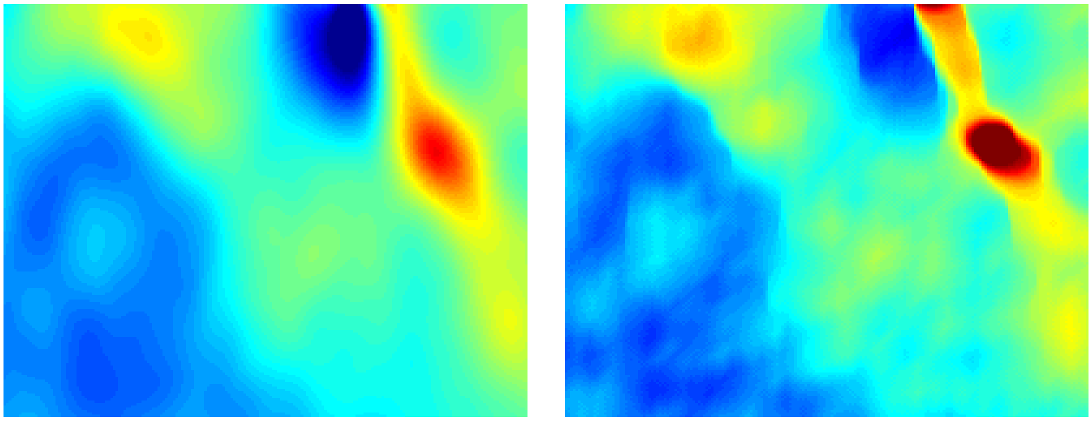

quadratic smoothness prior TV prior

Fig. 5. Quadratic smoothness prior versus TV prior (for the in vivo patient data). Using TV prior allows to obtain strain estimation which have sharper boundaries within the regions of high strain variation.

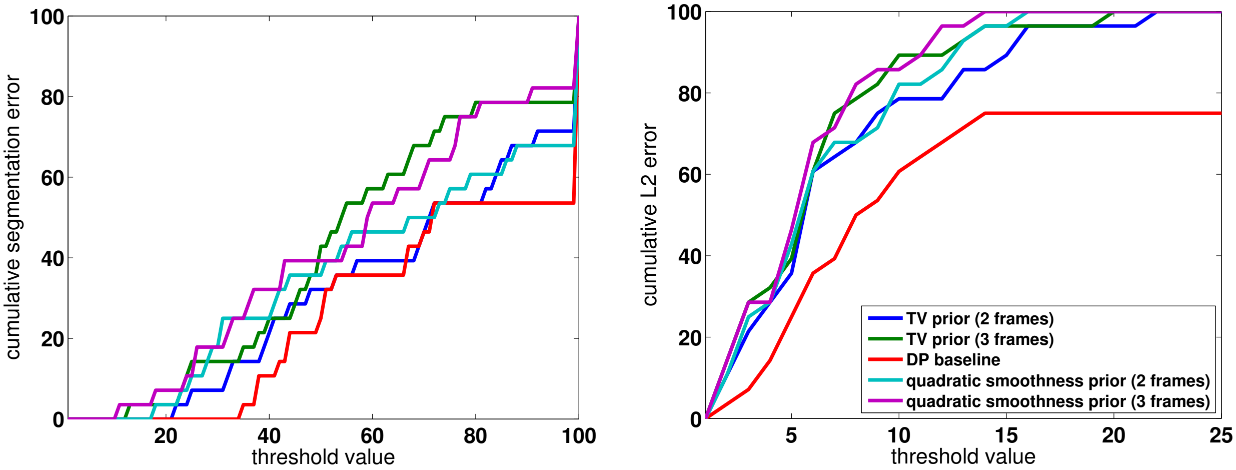

Fig. 6. Cumulative error plot for Jaccard index. Each of the graphs plots the fraction of the total inclusions number having the error measure i.e. L2 error and Jaccard index error less than the corresponding X-axis value. All four proposed methods significantly outperform the DP baseline, while triple-based methods perform better then their pair-based variations. The smoothness priors we consider demonstrate comparable quality according to the metrics of choice.

As it is seen from figure 8, the proposed triplet-based matching method produces the strain estimates with significantly higher effective contrast enabled by using greater compression ratios. Several additional soft and hard regions emerge on the strain map due to the utilization of the three-image algorithm. In addition, using a TV-prior effectively preserves the sharp boundaries on the strain image at the cost of introducing slight staircase effect that does not affect the diagnostic capabilities.

**Computational performance.** The computational time of the proposed method is composed of the block-matching search, which is executed twice, and the strain estimation algorithm. We use blocks of 100x4 pixels for the block-matching search and apply 9x7 median filter. The first stage of the block-matching algorithm is performed within 1% range of compression and second stage is performed with the reduced search range. From these considerations, we leave the efficient implementation of the block-matching algorithm beyond the scope of the current paper as it is currently performed in real-time in ultrasound elastography [30] (our serial MATLAB implementation currently takes approximately 3.5 sec in total to perform two block matching search procedures for the considered RF data dimensions).

The GPU implementation of the strain estimation algorithm was tested on a workstation with NVIDIA GTX 690 using CUDA 5.5 and takes 0.54 sec to compute the strain estimate for RF data frame of size 450x256 (1800x256 displacement map after 4:1 vertical down-sampling). Utilizing the mobile version NVIDIA GeForce GT 650M with CUDA 6.0 allows to compute the strain estimate in 0.98 sec for the considered image dimensions. The computational performance of the method enables potential clinical use as the image triplets themseleves typically take several seconds to be obtained for the hand-held probe.

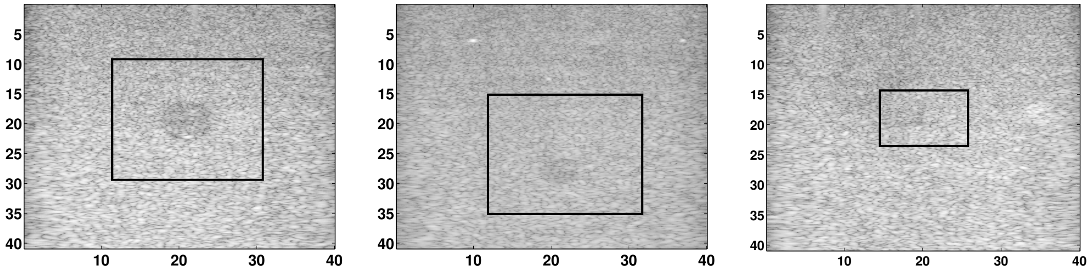

6 mm, B-mode image 4 mm, B-mode image 2 mm, B-mode image

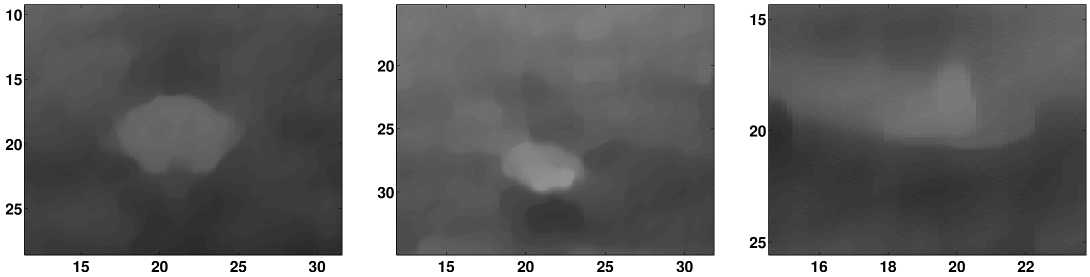

6 mm, 1% compr. (2 frames) 4 mm, 1% compr. (2 frames) 2 mm, 1% compr. (2 frames)

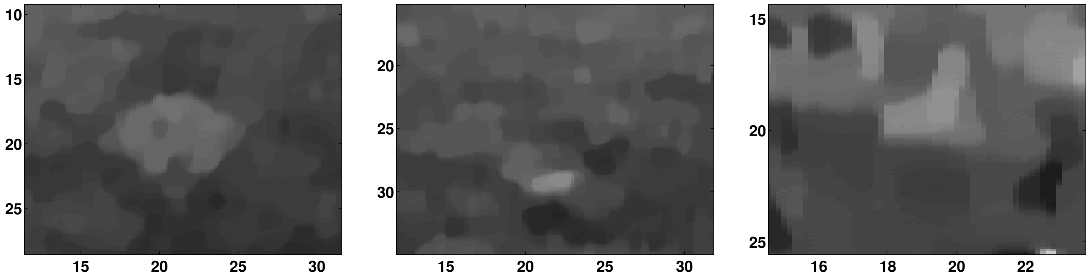

6 mm, 2% compr. (3 frames) 4 mm, 2% compr. (3 frames) 2 mm, 2% compr. (3 frames)

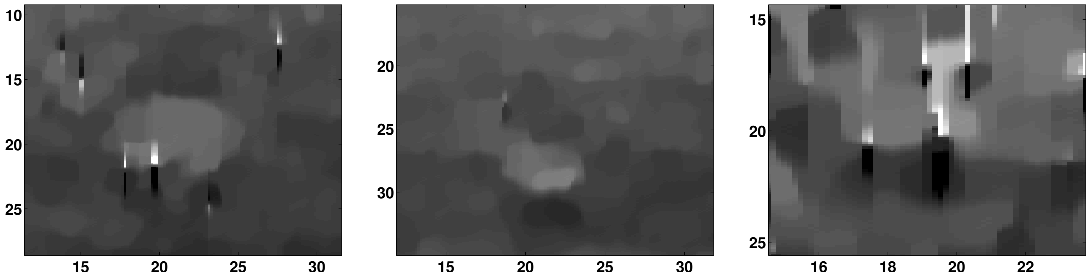

6 mm, 2% compr. (2 frames) 4 mm, 2% compr. (2 frames) 2 mm, 2% compr. (2 frames)

Fig. 7. Strain images for gelatin-agar phantoms with inclusions of 6,4,2 mm size (from the left to the right). First row: B-mode images, second row: the triplet-based method based on 2 frames with TV prior, third row: our method based on 3 frames with TV prior, fourth row: strain fields for the displacements computed directly for the second post-compression frame without using the triplet-based algorithm.

## VI. CONCLUSION

A new method for strain estimation in quasi-static ultrasound elastography from RF data is proposed. We use force-controlled ultrasound probe in our setup. Within the triplet-based algorithm, the less compressed frame effectively serves as a “stepping stone” that enables matching between the uncompressed and the more compressed frame. Smoothness-regularized (either TV or quadratic) energy functional is proposed for strain estimation. As a result, triplets of RF data frames are used to compute displacement estimates for 2-3% compression, which is unachievable using standard direct matching of frame pairs.

Our experiments thus demonstrate better performance of strain elastography when using triplets of RF data frames. This is supported by the quantitative measure of segmentation quality reported along with the L2 error for the set of simulated phantoms of stiff inclusion. The triplet-based matching shows a visible improvement for three real gelatine-agar phantoms of 2,4 and 6 mm size. Finally, we also observe better visibility of tumour in liver imaged before ablation when using triplets of RF data frames.

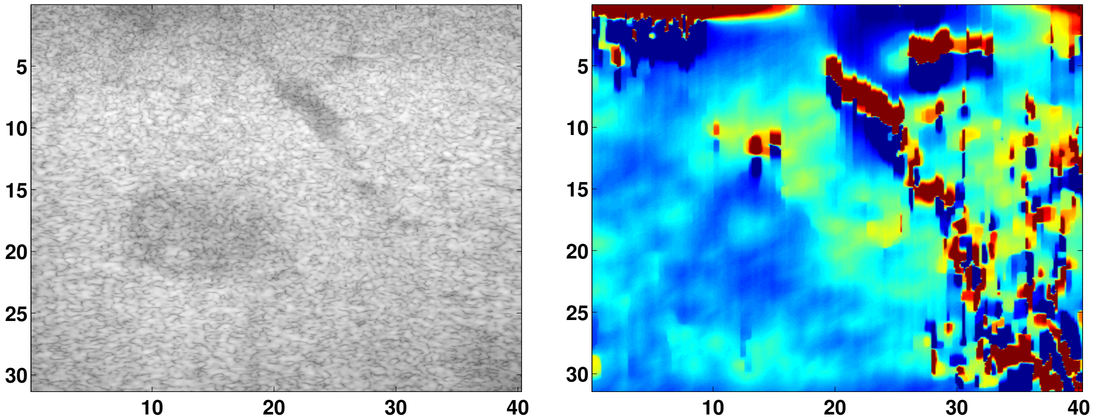

B-mode image

3% compression (2 frames)

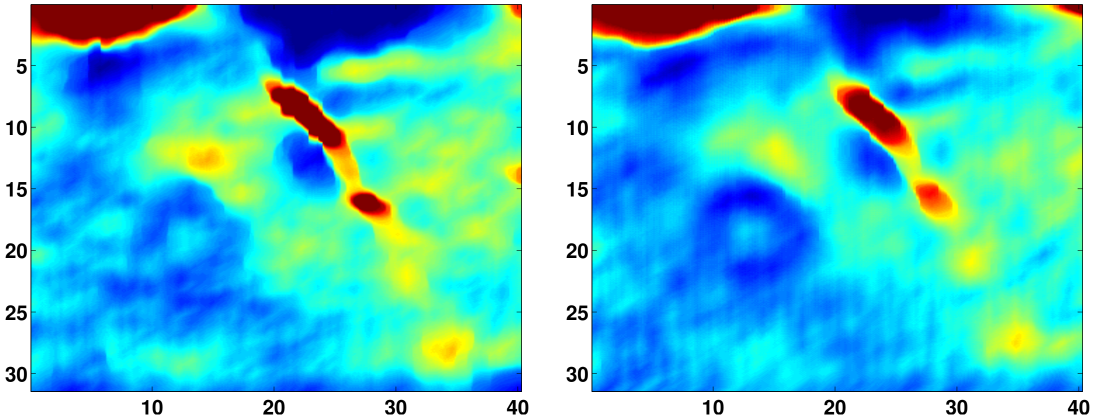

1.5% compression (2 frames)

3% compression (3 frames)

Fig. 8. Strain fields estimated for the tumor in liver. Our method demonstrates better performance as higher compression ratio is used. The tumour (large high strain region to the left from the image center) becomes more visible when using the triplet of RF data frames

## REFERENCES

[1] M. R. Burcher, J. A. Noble, L. Man, and M. Gooding, “A system for simultaneously measuring contact force, ultrasound, and position information for use in force-based correction of freehand scanning,” *Ultrasonics, Ferroelectrics and Frequency Control, IEEE Transactions on*, vol. 52, no. 8, pp. 1330–1342, 2005.

[2] M. Gilbertson and B. Anthony, “Ergonomic control strategies for a handheld force-controlled ultrasound probe,” *IEEE IROS*, pp. 1284–1291, 2012.

[3] J. Bamber and N. Bush, “Freehand elasticity imaging using speckle decorrelation rate.” *Acoust. Imaging*, vol. 22, pp. 285–292, 1996.

[4] J. Ophir, I. Cespedes, H. Ponnekanti, Y. Yazdi, and X. Li, “Elastography: a quantitative method for imaging the elasticity of biological tissues.” *Ultrason Imaging.*, vol. 13, no. 2, pp. 111–134, 1991.

[5] P. G. Brown, J. Alsousou, A. Cooper, M. S. Thompson, and J. A. Noble, “The autoqual ultrasound elastography method for quantitative assessment of lateral strain in post-rupture achilles tendons.” *Journal of Biomechanics*, vol. 46, pp. 2695–2700, 2013.

[6] H. Rivaz, E. Boctor, M. Choti, and G. Hager, “Real-time regularized ultrasound elastography.” *IEEE Trans. Medical Imaging*, vol. 30, no. 4, pp. 928–945, 2011.

[7] C. Pellot-Barakat, F. Frouin, M. Insana, and A. Herment, “Ultrasound elastography based on multiscale estimations of regularized displacement fields.” *IEEE Trans. Medical Imaging*, vol. 23, no. 2, pp. 153–163, 2004.

[8] F. Kallel and J. Ophir, “A least-squares strain estimator for elastography.” *Ultrason. Imaging.*, vol. 19, no. 3, pp. 195–208, 1997.

[9] T. J. Hall, P. E. Barbone, A. A. Oberai, J. Jiang, J. F. Dord, S. Goenezen, and T. G. Fisher, “Recent results in nonlinear strain and modulus imaging.” *Curr. Med. Imaging Rev.*, vol. 7, no. 4, pp. 313–327, 2011.

[10] J. Luo, J. Bai, P. He, and K. Ying, “Axial strain calculation using a low-pass digital differentiator in ultrasound elastography.” *IEEE Trans. Ultrason., Ferroelectr., Freq. Control.*, vol. 51, no. 9, pp. 1119–1127, 2004.

[11] U. Techavipoo and T. Varghese, “Wavelet denoising of displacement estimates in elastography.” *Ultrasound Med. Biol.*, vol. 30, no. 4, pp. 477–491, 2004.

[12] R. Chartrand, “Numerical differentiation of noisy, nonsmooth data.” *ISRN Applied Mathematics*, vol. 2011, 2011.

[13] A. DiBattista and J. A. Noble, “An efficient block matching and spectral shift estimation algorithm with applications to ultrasound elastography,” *Ultrasonics, Ferroelectrics and Frequency Control, IEEE Transactions on*, vol. 61, no. 3, pp. 407–419, 2014.

[14] H. Rivaz, E. Boctor, M. Choti, and G. Hager, “Ultrasound elastography using multiple images,” *Medical Image Analysis*, vol. 18, pp. 314–329, 2014.

[15] P. Chaturvedi, M. F. Insana, and T. J. Hall, “2-d companding for noise reduction in strain imaging,” *IEEE TUFFC*, pp. 179–191, 1998.

[16] J. Revell, M. Mirmehdi, and D. McNally, “Computer vision elastography: Speckle adaptive motion estimation for elastography using

ultrasound sequences." *IEEE Trans. Med. Imag.*, vol. 24, no. 6, pp. 755–766, 2005.

[17] K. Bredies, K. Kunisch, and T. Pock, "Total generalized variation," *SIAM J. Imag. Sc.*, vol. 3, pp. 492–526, 2010.

[18] F. Knoll, M. Unger, C. Diwoky, C. Clason, T. Pock, and R. Stollberger, "Fast reduction of undersampling artifacts in radial mr angiography with 3d total variation on graphics hardware," *Magn. Reson. Mater. Phy*, vol. 23, pp. 103–114, 2010.

[19] F. Knoll, K. Bredies, T. Pock, and R. Stollberger, "Second order total generalized variation (tgv) for mri." *Magn. Reson. Med.*, vol. 65, no. 2, pp. 480–491, 2011.

[20] M. Zhu and T. Chan, "An efficient primal-dual hybrid gradient algorithm for total variation image restoration," *UCLA CAM Report*, pp. 8–34, 2008.

[21] L. Rudin, S. Osher, and E. Fatemi, "Nonlinear total variation based noise removal algorithms," *Physica D: Nonlinear Phenomena*, vol. 60, no. 1, pp. 259–268, 1992.

[22] N. Bell and J. Hoberock, "Thrust: A productivity-oriented library for cuda," *GPU Computing Gems*, vol. 7, 2011.

[23] F. Kallel and J. Ophir, "A least-squares strain estimator for elastography," *Ultrasonic imaging*, vol. 19, no. 3, pp. 195–208, 1997.

[24] J. Jiang and T. J. Hall, "A generalized speckle tracking algorithm for ultrasonic strain imaging using dynamic programming," *Ultrasound in medicine & biology*, vol. 35, no. 11, pp. 1863–1879, 2009.

[25] I. Fleming, H. Rivaz, E. Boctor, and G. Hager, "Robust dynamic programming method for ultrasound elastography," *Proc. SPIE 8320*, 2012.

[26] J. A. Jensen and N. B. Svendsen, "Calculation of pressure fields from arbitrarily shaped, apodized, and excited ultrasound transducers," *IEEE Trans. Ultrasonics, Ferroelectrics and Frequency Control*, vol. 39, no. 2, pp. 262–267, 1992.

[27] J. A. Jensen, "Field: A program for simulating ultrasound systems," *10th Nordicbaltic Conference on Biomedical Imaging*, vol. 4, pp. 351–353, 1996.

[28] E. L. Madsen, M. A. Hobson, H. Shi, T. Varghese, and G. R. Frank, "Tissue-mimicking agar/gelatin materials for use in heterogeneous elastography phantoms," *Physics in medicine and biology*, vol. 50, no. 23, p. 5597, 2005.

[29] M. W. Gilbertson, "Handheld force-controlled ultrasound probe," Master's thesis, Massachusetts Institute of Technology, 2010.

[30] E. Montagnon, S. Hissoiny, P. Despres, and G. C., "Real-time processing in dynamic ultrasound elastography: A gpu-based implementation using cuda," in *Information Science, Signal Processing and their Applications (ISSPA), 2012 11th International Conference on*. IEEE, 2012, pp. 472–477.